

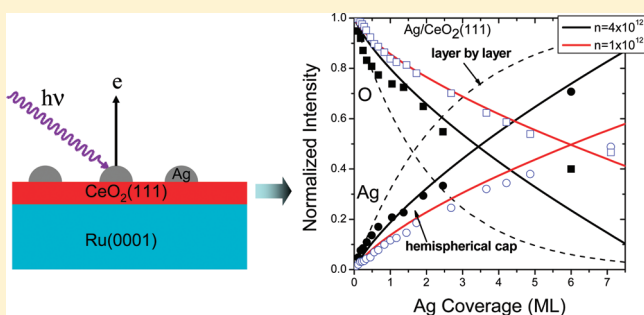
Growth, Structure, and Stability of Ag on CeO₂(111): Synchrotron Radiation Photoemission Studies

Dandan Kong,[†] Guodong Wang,[†] Yonghe Pan,[†] Shanwei Hu,[†] Jianbo Hou,[†] Haibin Pan,[†] Charles T. Campbell,[‡] and Junfa Zhu^{*,†}

[†]National Synchrotron Radiation Laboratory, University of Science and Technology of China, Hefei, Anhui 230029, P. R. China

[‡]Department of Chemistry, University of Washington, Seattle, Washington 98195-1700, United States

ABSTRACT: The growth and interfacial electronic properties of Ag on CeO₂(111) thin films have been studied by synchrotron radiation photoemission spectroscopy (SRPES), low energy electron diffraction (LEED), and X-ray photoelectron spectroscopy (XPS). Stoichiometric CeO₂(111) thin films were grown on a Ru(0001) substrate. Ag grows as three-dimensional (3D) particles on the well-ordered CeO₂(111) surface at 300 K with a number density of $\sim 1 \times 10^{12}$ particles/cm². When the CeO₂(111) surface has a high density of defects, Ag initially populates these defect sites, leading to a two-dimensional (2D) island growth at low coverages followed by 3D islanding at high coverages. The binding energy of Ag 3d increases when the Ag particle size decreases, which is mainly attributed to the final-state screening. No strong interaction between Ag and CeO₂(111) is found. The CeO₂(111) surface is slightly reduced upon Ag deposition, which can be ascribed to the reverse spillover of oxygen atoms from the Ag–CeO₂ boundary to the Ag nanoparticles. The Ag particles on CeO₂(111) experience significant sintering when the temperature increases before they desorb from the surface.



1. INTRODUCTION

Metal-on-oxide systems have received considerable attention because of their extreme importance in both fundamental research and technological applications, for instance, in micro-electronics devices, gas sensors, and heterogeneous catalysts.^{1–3} Interface properties referring to the interfacial diffusion, charge transfer, hybridization, morphology, and reactivity in the metal–oxide systems play crucial roles in determining their applications.^{4–11} In heterogeneous catalysis, ceria is one of the most important supports for metal catalysts, mainly the late transition metals, that have been widely used in a variety of catalytic reactions, such as CO and hydrocarbon oxidation, low-temperature water–gas shift reaction, automotive exhaust emission-control reactions, and low-temperature methanol synthesis.^{12–17} To gain fundamental insight into the interaction of metals with the CeO₂ support as well as their catalytic properties, substantial fundamental surface science studies in terms of the growth, structure, and reactivity of vapor-deposited metal nanoparticles on ordered CeO₂(111) surfaces have been performed.^{18–28} It is thought that the superb catalytic properties of the ceria-supported metal catalysts arise from: (1) the excellent redox properties of ceria (ceria is easily reduced and has high oxygen storage capacity)^{14,24} and (2) the stronger interactions of ceria with supported metal nanoparticles compared to other oxides, which can maintain smaller metal nanoparticles and resist the small particles to sinter into large particles under catalytic reaction conditions.¹¹ This is related to the easy

formation of defects, such as oxygen vacancies, on the ceria surfaces.

Among all the late transition metals, Ag is attractive for industrial applications due to its low cost and easy preparation. Ag supported on CeO₂ has been reported for use as electric contact materials²⁹ and in solid-oxide fuel cells.³⁰ In addition, it can be used as a catalyst in NO reduction, CO and hydrocarbon oxidation,³¹ methane oxidation,³² and formaldehyde oxidative decomposition.³³ Moreover, the use of Ag deposited on ceria was also found to increase the rate of carbon gasification in the oxidation of carbon soot particles compared to other noble metals.^{34–37} Despite these tremendous applications of the Ag/ceria system, the nature of the Ag–ceria interfaces in terms of interfacial morphologies, electronic/chemical properties, and interaction of Ag with ceria is still far from well understood. Recently, Farmer et al. employed adsorption microcalorimetry in combination with other techniques such as low-energy ion scattering (LEIS), Auger electron spectroscopy (AES), and low-energy electron diffraction (LEED) to study the adsorption energies and growth of Ag on the reduced CeO_{2-x}(111) ($x = 0.1–0.2$) thin films.^{11,20} A three-dimensional (3D) growth mode with a density of $\sim 4 \times 10^{12}$ particles/cm² for Ag on reduced CeO_{1.9}(111) was reported. The sticking probability of Ag on all reduced ceria surfaces was found to be near unity. In addition, the

Received: December 30, 2010

Revised: February 21, 2011

Published: March 15, 2011

higher heat of adsorption of Ag on the more reduced surfaces was attributed to stronger bonding of Ag particles to oxygen vacancies. Moreover, from the point of adsorption energetics they quantitatively explained why Ag has larger sinter resistance on $\text{CeO}_{2-x}(\text{111})$ than $\text{MgO}(\text{100})$, since it bonds much more strongly to $\text{CeO}_{2-x}(\text{111})$.¹¹ However, since they were not able to prepare the stoichiometric $\text{CeO}_2(\text{111})$ thin films, no results of Ag on $\text{CeO}_2(\text{111})$ were reported. Furthermore, to our knowledge, no studies of temperature-dependent thermal stability of Ag nanoparticles on CeO_2 can be found in the literature.

In this study, we use synchrotron radiation photoemission spectroscopy (SRPES) together with X-ray photoelectron spectroscopy (XPS) and LEED to investigate the growth, nucleation, and electronic properties of Ag on the ordered $\text{CeO}_2(\text{111})$ thin films which were prepared in situ on a $\text{Ru}(\text{0001})$ substrate. The advantage of the tunability of the photon energies enables us to investigate every core level and valence band with high sensitivity. In particular, in the case of a very low concentration of reduced state Ce^{3+} , from the Ce 3d spectra it is hard to determinate the extent of sample reduction since the changes in the spectra are difficult to quantify without extensive signal averaging.^{38–40} In contrast, valence band and Ce 4d spectra^{25,41,42} are very sensitive to the reduction of CeO_2 . From the core-level binding energies and Auger parameters, the electronic properties of the Ag/ CeO_2 interface with various sizes of Ag nanoparticles are determined. The thermal stability/sintering process of the Ag nanoparticles with different initial sizes at elevated temperature are also studied.

2. EXPERIMENTAL SECTION

All the experiments were performed at the Photoemission Endstation at beamline U20 in the National Synchrotron Radiation Laboratory, Hefei, China. This beamline is connected to a bending magnet and equipped with three gratings that cover photon energies from 60 to 1000 eV with a resolving power ($E/\Delta E$) better than 1000. The endstation consists of an analysis chamber and a sample preparation chamber, whose base pressures are 2×10^{-10} and 5×10^{-10} Torr, respectively, and a sample load-lock system. The analysis chamber is equipped with a VG Scienta R3000 electron energy analyzer, a twin anode X-ray source, rear-view LEED optics, a quadrupole mass spectrometer (Pfeiffer QMS220), and an Ar^+ sputter gun. The preparation chamber is connected with a quick load-lock port and houses an e-beam evaporator for Ce and a home-built evaporator for Ag.

The photoemission spectra were recorded at normal emission and have been normalized to the photon flux which was calibrated by measuring the Au 4f spectra from a clean Au foil attached to the sample holder. The following photon energies have been used to probe the different core levels: Ru 3d, 650 eV; Ce 4d, 450 eV; Ag 3d, 650 eV; O 1s, 650 eV. Valence band spectra were recorded with a photon energy of 170 eV. Binding energies (BEs) were calibrated with respect to the Au 4f_{7/2} (BE = 84 eV) feature from the Au foil, which was measured immediately after each spectrum.

The $\text{Ru}(\text{0001})$ single crystal (10 mm diameter and 2 mm thickness) sample, purchased from MaTeck GmbH, Germany, was used as the substrate. The sample was mounted on a Mo sample holder which was fixed by Ta wires at the side. A K-type thermocouple was used to monitor the sample temperature. The sample was cleaned by repeated cycles of Ar^+ bombardment at room temperature followed by annealing up to 1300 K until no

contaminants were detected by XPS and a sharp LEED pattern was observed.

$\text{CeO}_2(\text{111})$ thin films were prepared following a recipe similar to that reported previously.^{43,44} Briefly, the epitaxial grown ordered $\text{CeO}_2(\text{111})$ films were produced by evaporating cerium metal in 2×10^{-7} Torr oxygen environments onto $\text{Ru}(\text{0001})$ with a constant substrate temperature of 700 K. To promote film ordering to form large flat terraces, the films need to be postannealed at 980 K in oxygen.⁴⁴ In this study, the $\text{CeO}_2(\text{111})$ films after growth were postannealed at 980 K in oxygen, unless otherwise specified. Metallic cerium (99.99%, Goodfellow) was evaporated from an electron bombarded W crucible using a water-cooled e-beam evaporator that was equipped with an integral flux monitor, enabling real-time control of the deposition rate. The growth rate of the CeO_2 films was estimated, from the attenuation of the Ru 3d signal at a photon energy of 650 eV, to be 0.089 ± 0.003 nm/min by assuming the electron mean free path of 1 nm.^{43,45} The thickness of the $\text{CeO}_2(\text{111})$ films is about 4 nm. With this thickness, the long-range electronic interaction effect with the underlying $\text{Ru}(\text{0001})$ substrate can be neglected, as reported by Farmer et al.^{11,20} One CeO_2 monolayer (ML) is defined as 7.89×10^{14} CeO_2 units per cm^2 , which is the number of oxygen atoms per unit area in the topmost atomic layer of the $\text{CeO}_2(\text{111})$ surface (which is terminated in an open oxygen layer with a layer of coordinatively-unsaturated Ce^{4+} ions below).²⁰ Dividing this by the density of bulk ceria (2.53×10^{22} CeO_2 units per cm^3) gives the thickness of a CeO_2 monolayer to be 0.31 nm.

Ag was deposited onto the ceria films by evaporating Ag metal (99.999%, Alfa Aesar) from a tantalum basket, which was thoroughly degassed prior to use. The deposition rate of Ag, estimated from the attenuation of Ru 3d signals at a photon energy of 650 eV after Ag was directly deposited onto $\text{Ru}(\text{0001})$, was 0.069 ± 0.002 ML/min. One monolayer (ML) of Ag is defined throughout as the number of Ag atoms per area in a closed-packed layer (111) of Ag atoms with lattice parameter of bulk Ag (1 ML = 1.4×10^{15} atoms/ cm^2), which is about twice the number of oxygen atoms in $\text{CeO}_2(\text{111})$ exposed to the vacuum per unit area.²⁰

3. RESULTS

3.1. Characterization of the $\text{CeO}_2(\text{111})$ Films. Figure 1 shows the Ce 4d and valence band (VB) spectra for a 4 nm thick fully oxidized $\text{CeO}_2(\text{111})$ film grown on $\text{Ru}(\text{0001})$, along with spectra from a typical partially reduced CeO_{2-x} film for comparison. The reduced CeO_{2-x} film was obtained by annealing the CeO_2 film at 1000 K for 10 min. Both Ce 4d and VB spectra from the oxidized $\text{CeO}_2(\text{111})$ surface are very similar to those reported previously.⁴³ In the Ce 4d region, the two peaks located at 125.2 and 121.9 eV, respectively, are only related to the presence of Ce^{4+} .^{43,46} They vanish when the surface is fully reduced to $\text{CeO}_{1.5}$.⁴³ Therefore, the intensities of these two peaks can be directly used to calculate the extent of reduction assuming a linear relationship of the changes in intensities of these two peaks against the relative amount of Ce^{4+} . In the valence band region, only the contribution from O 2p is observable. The absence of a Fermi edge is indicative of neither metallic Ce nor substrate Ru being visible on the surface. For the thermally reduced CeO_{2-x} ($x = 0.15$) film the intensities of the peaks at 125.2 and 121.9 eV in the Ce 4d spectrum are only 70% of those for the CeO_2 film, implying that $\sim 30\%$ of the Ce^{4+} has been reduced to Ce^{3+} on the surface. The appearance of the

distinct Ce 4f peak at 1.5 eV, which is only related to the amount of Ce^{3+} ,⁴³ in the valence band further confirms the existence of a high concentration of Ce^{3+} on the reduced CeO_{2-x} film. Note that Figure 1b differs slightly in peak intensities from the results of Mullins et al.,⁴³ which can be attributed to the different excitation photon energies we used here, since both the relative photoionization cross sections and probe depth vary with the photon energies significantly.^{47,48}

Figure 2 shows LEED patterns for different thicknesses of $\text{CeO}_2(111)$ grown on Ru(0001). The clean Ru(0001) surface exhibits a sharp $p(1 \times 1)$ LEED pattern, as shown in Figure 2(a). After growth of 1 nm (3 ML) of CeO_2 , in addition to the original spots from Ru(0001), some new spots with smaller distance to the (0,0) spot compared to the original first-order spots of Ru(0001) are clearly observed as a hexagonal structure. This is the well-known $p(1.4 \times 1.4)$ LEED pattern of $\text{CeO}_2(111)$ with respect to the $p(1 \times 1)$ pattern of clean Ru(0001) (shown in Figure 2(b)), as expected based on prior observations.⁴³ With increasing thickness of the CeO_2 film, the $p(1.4 \times 1.4)$ spots further intensify at the expense of the $p(1 \times 1)$ spots of Ru(0001). When the CeO_2 film reaches 2 nm thickness, the LEED pattern from the Ru substrate can no longer be observed, and only the pattern from the $\text{CeO}_2(111)$ film is observed. Shown in Figure 2(c) is a sharp $p(1.4 \times 1.4)$ LEED pattern which corresponds to a (1×1) pattern of $\text{CeO}_2(111)$ obtained from a 4 nm thick $\text{CeO}_2(111)$.

3.2. Growth of Ag on $\text{CeO}_2(111)$ at Room Temperature. The dispersion, nucleation, and wetting properties of metals on

oxides are of great interest in heterogeneous catalysis. Study of the growth mode of ultrathin metal films on well-defined oxide surfaces provides important insights into the nature of the bond between metal and oxide surfaces. STM studies revealed that on the ordered $\text{CeO}_2(111)$ films the deposition of Au, Pd, Rh, and Pt at 300 K follows a three-dimensional (3D) growth mode.^{21,22,26} At low Au coverages (<0.1 ML), Weststrate et al.⁴⁵ observed that Au prefers to grow two-dimensionally on $\text{CeO}_2(111)$. In the present study, SRPES was used to investigate the growth mode of Ag on $\text{CeO}_2(111)$ by monitoring the intensity changes of Ag 3d and O 1s. We have studied the growth of Ag on two different 4 nm thick $\text{CeO}_2(111)$ films with different roughness. The two $\text{CeO}_2(111)$ films were prepared with and without postannealing at higher temperature (980 K) in oxygen environments, respectively. According to the STM studies,⁴⁴ due to large lattice mismatch (40%) between $\text{CeO}_2(111)$ and Ru(0001), smooth and well-ordered CeO_2 films can be only obtained by further annealing at higher temperatures. The ceria films become better ordered and have much larger terraces after postannealing in oxygen at higher temperatures.⁴⁴ The $\text{CeO}_2(111)$ film without postannealing shows particle-like features and, of course, has higher concentration of defects (step edges and kinks). However, from the conventional LEED observations, the differences in the morphology of these two films can hardly be discriminated, in line with previous literature results.⁴⁴ In addition, both CeO_2 surfaces should have low density of point defects (oxygen vacancies) on the terraces.⁴⁴

As shown in Figure 3, the solid points represent the data from the $\text{CeO}_2(111)$ surface without postannealing, while the hollow data points were obtained from the surface with postannealing. On both surfaces, the normalized intensity changes of the Ag 3d_{5/2} and O 1s peaks are plotted as a function of Ag coverage, respectively. Here, the intensities of Ag 3d_{5/2} and O 1s are normalized to those of bulk-like Ag and clean $\text{CeO}_2(111)$, respectively. As can be seen, on both $\text{CeO}_2(111)$ surfaces the intensity of the Ag 3d_{5/2} peak increases continuously with increasing Ag coverage, and simultaneously that of the O 1s peak decreases. To clarify the growth mode, we calculated the expected results for both a layer-by-layer growth mechanism⁴⁹ and a simple 3D-particle (hemispherical cap) growth model,^{50,51} shown as the dashed lines and the solid curves, respectively. The 3D growth model assumes that the Ag particles have hemispherical shapes and constant island density with uniform radii. The island density is independent of coverage and treated as a fitting parameter (here we use the best fitted island densities of $\sim 4 \times 10^{12}$ and $\sim 1 \times 10^{12}$ particles/cm² for the $\text{CeO}_2(111)$ films without and with postannealing at higher temperature in oxygen, respectively). Therefore, at any given Ag coverage the average particle volume and diameter can be calculated. For example, at a coverage of 1 ML, the average

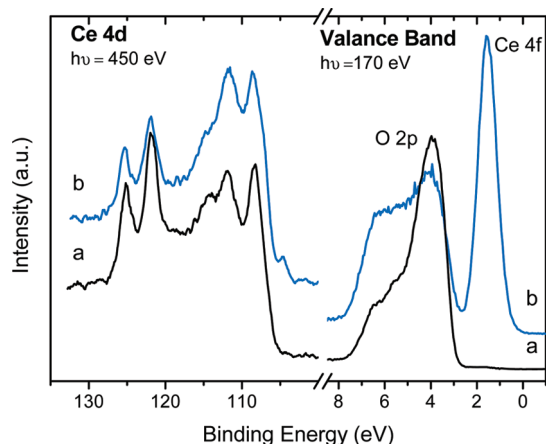


Figure 1. Ce 4d and valence band spectra for (a) a 4 nm thick $\text{CeO}_2(111)$ film grown on Ru(0001) and (b) after annealing this $\text{CeO}_2(111)$ film at 1000 K in vacuum for 10 min, resulting in a reduction of surface with the approximate surface stoichiometry of $\text{CeO}_{1.85}$. The Ce^{3+} concentration was calculated using the Ce 4d spectra.

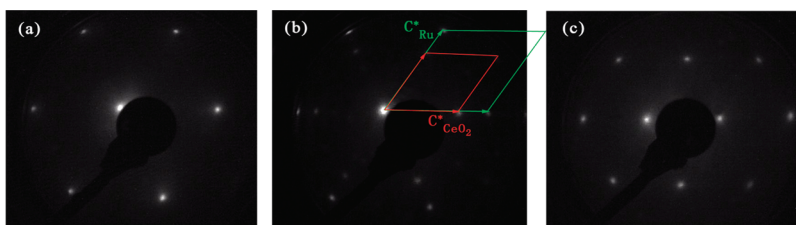


Figure 2. LEED patterns taken from (a) clean Ru(0001), $E_p = 91$ eV; (b) 1 nm (~ 3 ML) $\text{CeO}_2(111)$, $E_p = 90$ eV; (c) 4 nm $\text{CeO}_2(111)$, $E_p = 90$ eV. The (0,0) spot is near the center of the screen. In (b), the unit cells of $\text{CeO}_2(111)$ and Ru(0001) are indicated.

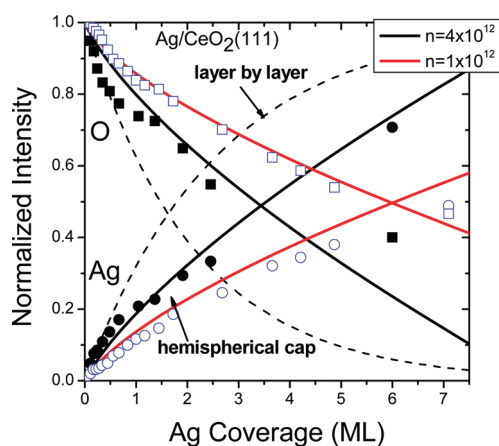


Figure 3. Integrated Ag 3d_{5/2} (circles) and O 1s (squares) XPS peak intensities, normalized to bulk Ag and the clean CeO₂(111) surface, respectively, versus coverage for Ag growth on 4 nm thick CeO₂(111) films at room temperature. The solid data points represent the results from the CeO₂(111) film without postannealing at higher temperature in oxygen, while the open data points are the results obtained from the CeO₂(111) film with postannealing at 980 K in oxygen. The dashed curves correspond to what is expected if Ag grows in a layer-by-layer growth mode, and the solid curves represent a hemispherical cap model with constant island densities (4×10^{12} and 1×10^{12} islands/cm² for the CeO₂(111) films without and with postannealing at higher temperature in oxygen, respectively). The inelastic mean free path used for calculating the curves is 0.61 nm for Ag and 0.5 nm for O, obtained from ref 52, and the detection angle was 0°.

particle size is calculated to be 3.0 nm in diameter on the CeO₂(111) films without postannealing at higher temperature in oxygen.

As seen in Figure 3, on the CeO₂(111) surface without postannealing during the early stage of Ag growth (<0.3 ML), the Ag signal changes along a slope very close to that expected for a layer-by-layer growth or two-dimensional (2D) growth. In parallel, the substrate O signal decreases with a slope also in accord with that of the expected 2D growth. As the Ag coverage increases to above 0.3 ML, both the substrate and overlayer signals deviate from the layer-by-layer growth mode and rapidly exhibit behavior indicative of 3D island growth with an island density of $\sim 4 \times 10^{12}$ islands/cm². Even at the coverage above 6 ML, the O signal can be still clearly seen, implying that a large fraction of the substrate area is still exposed; this is clear evidence for the 3D growth of Ag on the surface. This 2D–3D transition in the growth mode of Ag on CeO₂(111) is similar to those reported for Ag/TiO₂, Ag/SiO₂, and Ag/MgO systems^{53–56} but in contrast to that of Ag on reduced CeO_{2–x}(111) where only 3D growth was found.²⁰

In contrast, on the CeO₂(111) surface with postannealing both the Ag 3d and O 1s signals indicate that the growth of Ag exhibits 3D behavior during the initial growth stages. In addition, the particles have smaller island density ($\sim 1 \times 10^{12}$ islands/cm²) in comparison with those on the surface without postannealing. This means that at a given Ag coverage the mean particle sizes are larger on the better ordered CeO₂(111) surface than on the rough CeO₂(111) surface. In other words, when the CeO₂(111) surfaces have more defects the Ag particles grow smaller and are better dispersed, as we observed. Similar results have been found by Weststrate et al.²⁵ for Au on CeO₂(111) where Au grows with smaller average diameters on the rough

CeO₂ surface compared with the smooth surface. It is common that metal nucleates at the defect sites of the oxide surfaces at very low coverages, undergoing a 2D growth.^{22,26,44,51,57} Since the CeO₂(111) surfaces have low density of point defects, i.e., oxygen vacancies,⁴⁴ it is very likely that Ag preferentially nucleates on the defect sites such as step edges and kink sites initially. After these defect sites are populated, Ag starts to grow three-dimensionally on the surface. On the better ordered surfaces, the density of the defects is much lower, thus the nucleation sites are much less for Ag growth. Therefore, the island density is much lower, and at the same coverage the Ag particle sizes are much larger.

It is of interest to compare the growth mode we derive from experimental data with that predicted from thermodynamic parameters. As we know, if the interfacial energy ($\gamma_{m/o}$) is smaller than the difference between oxide surface energy ($\gamma_{v,o}$) and deposited metal surface energy ($\gamma_{v,m}$), i.e., $\gamma_{m/o} < \gamma_{v,o} - \gamma_{v,m}$, the metal is energetically favored to wet the oxide surface.² Otherwise, 3D growth occurs. The criterion can also be expressed in terms of metal–oxide adhesion energy, E_{adh} . If it exceeds the adhesion energy of metal–metal, one would expect that the metal will wet the oxide surface and form a continuous film. Since the adhesion energy of Ag nanoparticles to the reduced CeO_{1.9}(111) surface is ~ 2.3 J/m² and becomes even larger on more reduced surfaces,¹¹ it is expected that the adhesion energy of Ag nanoparticles to the oxidized CeO₂(111) surface is smaller than 2.3 J/m². This value is obviously less than the adhesion energy of Ag to itself (2.44 J/m²),^{11,58} therefore, one would expect that the growth of Ag on CeO₂(111) follows 3D mode, consistent with our results. However, on the rough CeO₂(111) surface where the concentration of defects (step edges and kinks) is higher than that on a better ordered surface, a Ag particle bonds locally to these defect sites with an adhesion energy which is likely much more than the stoichiometric CeO₂ terraces. This would result in Ag being more thermodynamically favored to form 2D islands in the initial stages of Ag growth.

Note that although the growth models are strongly supported by both the experimental results and thermodynamic prediction it would be helpful to further confirm these by STM observations which provide more direct structural/morphological information.

3.3. Interfacial Electronic Properties. The electronic, optical and magnetic properties of metal nanoparticles supported on oxide supports can diverge strongly from those of the bulk materials.⁵⁹ The interactions between metal particles and oxide supports have been widely studied using photoelectron spectroscopy. When metal particles are deposited on oxide surfaces, binding energy shifts in core-level spectra are often observed as a function of particle size, which can be interpreted as being due to either initial^{60–62} or final state effects or both.^{63,64} In general, initial state effects can be attributed to reduced metal–metal coordination and/or metal–oxide interaction, while final state effects arise from final state screening, i.e., relaxation effects, which depend on the shape and size of the particles as well as the supports.^{61,65} However, separating the relative contributions of these two effects on the core-level binding energy shifts is an issue.

Here we use the Auger parameter method which was first introduced by Wagner⁶⁶ to shed light onto the origin of the particle-size-dependent Ag 3d level shifts. In Figure 4a and 4b, the Ag 3d_{5/2} core level binding energy and Ag M₅VV Auger transition kinetic energy are plotted as a function of Ag coverage

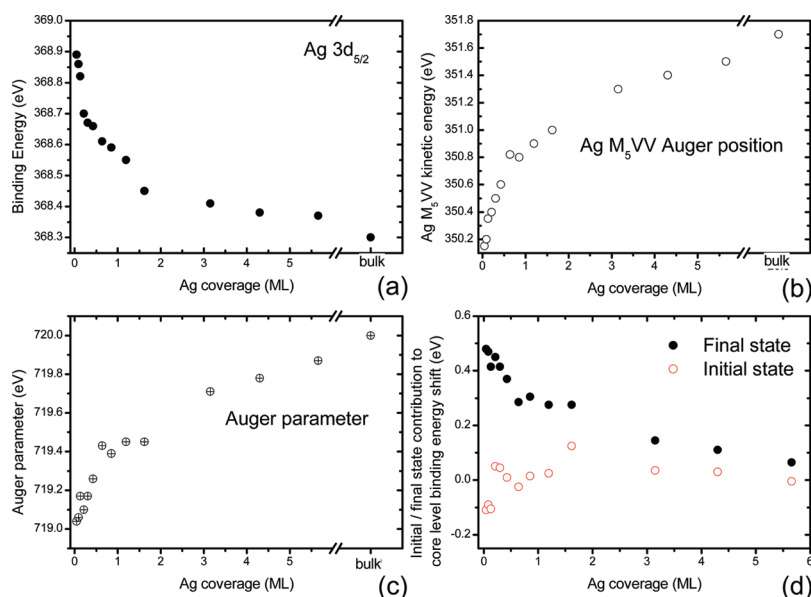


Figure 4. (a) Ag 3d_{5/2} core level binding energy; (b) Ag M₅VV Auger peak kinetic energy; (c) Auger parameter; and (d) initial state and final state contribution to the core level binding energy shifts as a function of Ag coverage on CeO₂(111) at 300 K. The total core level shifts come from $\Delta\epsilon - \Delta R$, where $\Delta\epsilon$ and ΔR represent the initial state and final state contributions, respectively.

at 300 K. As can be seen, with decreasing Ag coverage, the Ag 3d_{5/2} binding energy shifts to a higher BE, while the kinetic energy (KE) of the M₅VV Auger transition shifts to a lower KE. At 0.04 ML Ag coverage, with respect to the bulk Ag value, the Ag 3d BE is higher by 0.6 eV and the M₅VV Auger peak position is lower by 1.5 eV. Above 10.0 ML Ag coverage, they all approach the bulk Ag value.

It was previously shown by Wagner that the sum of the kinetic energy shift of the Auger peak and the binding energy shift of the core level peak approximately equals twice the final state contributions to the core level shifts.^{66–68} This can be rationalized only when the energy shifts of different orbitals are the same. For Ag clusters grown on alumina surfaces, Luo et al.⁶⁹ have demonstrated the validity of the Wagner analysis by the observation of parallel shifts of the Ag 3d peak and the center of the Ag 4d band. The Auger parameter (α), which is currently defined as the sum of the Ag 3d_{5/2} core level binding energy (shown in Figure 4a) and the kinetic energy of the M₅VV Auger transition (shown in Figure 4b), is plotted as a function of Ag coverage in Figure 4c. The Auger parameter increases with increasing Ag coverage and shows opposite shifts from the Ag 3d core levels. The value of α increases from 719.6 to 721.6 eV with increasing Ag coverage from 0.04 ML to the bulk value. As mentioned above, the final state contribution (ΔR) to the Ag 3d_{5/2} core level BE shifts can be written as

$$\Delta R = \Delta\alpha/2 \quad (1)$$

The shift in the Auger parameter ($\Delta\alpha$) can be estimated from the data shown in Figure 4c. The initial state contribution ($\Delta\epsilon$) can be calculated by

$$\Delta\epsilon = \Delta BE + \Delta R \quad (2)$$

The resulting values for ΔR and $\Delta\epsilon$ are plotted as a function of Ag coverage in Figure 4d. It is obvious that over the entire coverages we investigated the final state contribution (ΔR) to the Ag 3d core level binding energy shifts is dominant. At very low

coverage (0.04 ML), the final state effects contribution is calculated to be ~ 0.5 eV, while the initial state contribution ($\Delta\epsilon$) is about -0.1 eV. When the Ag coverage increases to ~ 0.2 ML, the initial state contribution becomes negligible, and only the final state contribution accounts for the Ag 3d BE shifts.

It is known that the final state effects originate from the screening and relaxation of the core hole created by photoemission, which depends on the shape and size of the metal particles as well as on the substrate. Due to the poor conductivity and coupling of the substrate with the metal particle, the hole created by photoemission can not be compensated by the transfer of a screening electron from the substrate to the metal particle. As a result, the kinetic energy of escaping photoelectron is lowered due to the Coulomb interaction between the escaping electron and the remaining hole, leading to the observed BE shifts. The initial state effects arise from the electron charge transfer between metal and substrate and/or intrinsic size effects due to reduced metal–metal coordination in the metal particles. Since the direction and the value of the initial state shifts are consistent with the surface core level shifts (SCLS) of Ag (-0.15 eV for Ag(111)⁷⁰), this initial state contribution can be attributed to a reduced average coordination number for Ag atoms in small particles. Electron charge transfer from Ag to CeO₂ resulting in the formation of positively charged Ag⁺ is unlikely because, although the oxidation of Ag would lead to negative BE shifts of the Ag 3d core level relative to the metallic Ag state, a much larger BE shift is expected if Ag is positively charged (for Ag₂O and AgO, -0.4 and -0.8 eV shifts relative to metallic Ag 3d were observed, respectively.⁷¹). On the other hand, since Ag bonds more strongly on the defect sites, positively charged Ag would be even more easily observed. However, on the CeO₂(111) film without postannealing, we found that the initial state effect contribution to the Ag 3d BE shifts during Ag growth is essentially very small and can be negligible. Therefore, it is conclusive that charge transfer between Ag and CeO₂ does not occur to a measurable extent during the Ag growth on CeO₂(111). In other words, Ag particles maintain metallic states on the

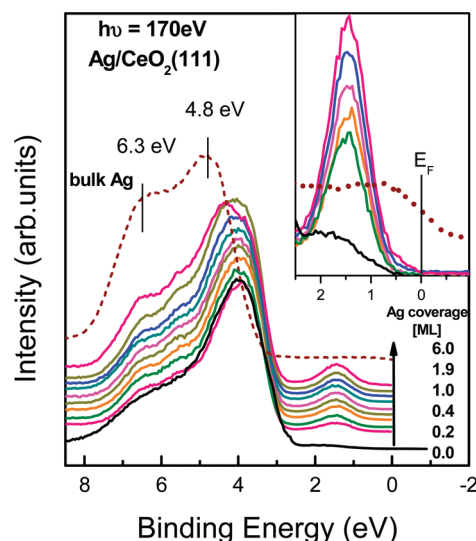


Figure 5. Valence band photoemission spectra of Ag on $\text{CeO}_2(111)$ as a function of Ag coverage taken at a photon energy of 170 eV. The dashed curve represents a bulk-like Ag thick film. A broad and unresolved feature in the BE range from 3 to 8 eV observed from the clean $\text{CeO}_2(111)$ (bottom spectrum) comprises mainly O 2p states. The inset shows the detailed changes of Ce 4f, from which an increase in Ce^{3+} concentration is observed.

$\text{CeO}_2(111)$ surface. Similar results have been reported for Ag on $\text{Al}_2\text{O}_3/\text{Re}(0001)$.^{69,72} However, our results are in contradiction to previous results for 1% Ag/ CeO_2 ⁷³ and density functional theory (DFT) calculations for Ag on $\text{CeO}_2(111)$,¹⁸ where positive-charged ionic Ag^+ was reported. It is worth pointing out that from pure XPS studies it is difficult to distinguish between Ag^+ and metallic Ag^0 due to the lower binding energy shift of Ag^+ compared to Ag^0 from the Ag 3d core level only, particularly when the particle size is in the nanometer scale.

Figure 5 shows the valence band spectra for Ag deposited on $\text{CeO}_2(111)$ at different Ag coverages. The main feature of the spectrum from the clean substrate (bottom curve) is the broad peak ranging from 3 to 8 eV which can be ascribed to O 2p structure.⁴³ With increasing Ag coverage, this broad peak shifts to the higher binding energy side due to the coupling of Ag states. In addition, a peak located at ~ 1.5 eV below the Fermi level (E_F), which is attributed to Ce 4f,⁴³ gradually increases in intensity. As mentioned above, this peak is only related to the reduced state Ce^{3+} . The appearance of this state as well as its gradual increase in intensity, as can be clearly seen in the inset of Figure 5, indicates that the CeO_2 surface is reduced upon Ag deposition.

Moreover, the density of state (DOS) near E_F gradually increases with increasing Ag coverage. For comparison, the valence band spectrum from a bulk-like Ag film (>40 ML) is shown as the dashed curve in Figure 5, where a prominent feature at 4.8 eV and a second feature centered at 6.3 eV, as well as a sharp Fermi edge (seen in inset of Figure 5), are observed. The features at 4.8 and 6.3 eV can be attributed to the 4d band state of metallic Ag.^{74,75}

It is worth mentioning that in previous studies a new state at ~ 1.2 eV near the E_F was observed with increasing Ag cluster size on amorphous graphite, which was primarily ascribed to the 5s state since Ag has a nearly filled 4d state.⁷⁶ However, this 5s state was only observable when the Ag coverage was larger than 8.5×10^{15} atoms/ cm^2 (in our case it corresponds to 6 ML). It primarily

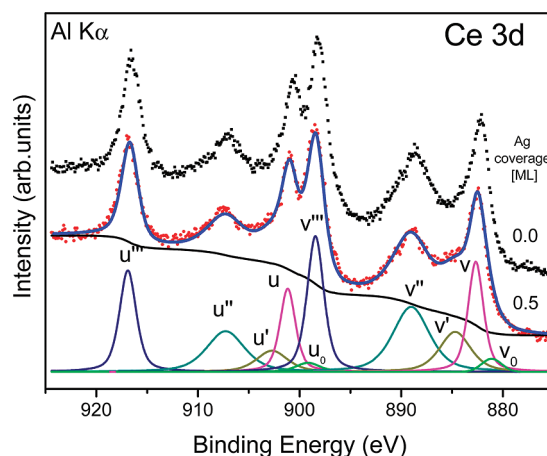


Figure 6. Ce 3d XPS spectra excited by Al $K\alpha$ radiation from a clean 4 nm thick $\text{CeO}_2(111)$ thin film surface and the surface covered with 0.5 ML Ag at room temperature. Dots: experimental data. Solid lines: Shirley-type background and fitted peaks: u' , u_0 , v' , and v_0 are related to Ce^{3+} , and the rest are due to Ce^{4+} .

appeared at around 2.1 eV for small particles.⁷⁶ In our experiment, we can rule out the possibility of the increase in Ce 4f intensity induced by the appearance of the Ag 5s state since at very low Ag coverage (<0.4 ML) where the Ag 5s state should have negligible intensity the increase in Ce 4f intensity has already been observed, and moreover, there is no shift of the Ce 4f peak position. Therefore, it is clear that CeO_2 has been reduced after Ag deposition. Further evidence can also be provided by the observation of Ce 3d core-level spectra. Figure 6 shows the Ce 3d XPS spectra acquired from a clean $\text{CeO}_2(111)$ surface as well as the surface covered by 0.5 ML Ag. The spectra exhibit evident changes after Ag deposition. Decomposition of the spectrum for 0.5 ML Ag covered $\text{CeO}_2(111)$ is presented at the bottom of Figure 6. The appearance of new spectral components at 885.0 and 880.5 eV is clear evidence of the formation of Ce^{3+} ions.^{40,77}

The detailed mechanism for the reduction of CeO_2 upon Ag deposition will be discussed later. Here we first rule out the possibility of the reduction being caused by photon-induced desorption of oxygen atoms from the $\text{CeO}_2(111)$ surface through a control experiment. We performed this experiment on a 0.1 ML Ag covered $\text{CeO}_2(111)$ by measuring the valence band spectra with a different dosage of synchrotron radiations. The results show no difference in the valence band spectra between the fresh-prepared sample and the sample after exposing it for a long time to synchrotron radiations, indicating that the formation of the Ce^{3+} state does not result from photon-induced desorption of O atoms from $\text{CeO}_2(111)$.

3.4. Thermal Sintering. For Au, Pd, and Pt on $\text{CeO}_2(111)$,^{19,22,78} it has been reported that annealing in UHV leads to significant sintering of metal particles on the surface. Even heating up to 500 K, Au nanoparticles experience an increase in particle size on $\text{CeO}_2(111)$.^{19,21} To determine the thermal stability of Ag nanoparticles on CeO_2 , we have carried out the following experiments.

Two different coverages of Ag deposited on $\text{CeO}_2(111)$ at 300 K were annealed at elevated temperatures, after which Ag 3d spectra were collected at 300 K. In Figure 7(a), the Ag $3d_{5/2}$ peak intensities are plotted as a function of temperature for Ag/

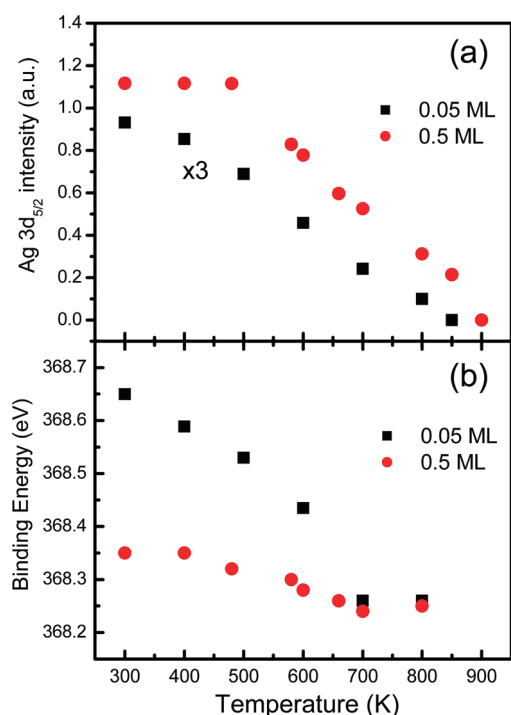


Figure 7. (a) Ag 3d_{5/2} peak intensities for 0.05 and 0.5 ML Ag on CeO₂(111) as a function of annealing temperature. (b) Binding energies of Ag 3d_{5/2} spectra for 0.05 and 0.5 ML Ag on CeO₂(111) as a function of annealing temperature. The spectra were collected at 300 K.

CeO₂(111) samples with 0.05 and 0.5 ML Ag coverage, respectively. As expected, the intensity of the Ag 3d_{5/2} peak for 0.5 ML Ag on CeO₂(111) at 300 K is much higher than that of 0.05 ML. Correspondingly, the particle size is also much larger for 0.5 ML Ag. With increasing annealing temperature, the Ag 3d_{5/2} intensity for 0.05 ML Ag/CeO₂(111) starts to decrease already at 400 K, while for 0.5 ML the Ag 3d_{5/2} intensity remains nearly unchanged up to 500 K. When the temperature is higher than 500 K, the Ag 3d_{5/2} intensities from both surfaces decrease rapidly. At about 900 K, no Ag signal can be detected.

In principle, there are three possible reasons which account for the decrease of Ag 3d_{5/2} intensity during annealing: (i) small Ag particles agglomerate into large particles, i.e., sintering; (ii) Ag diffuses into the subsurface; and (iii) Ag desorbs from the surface. For metal supported on oxide surfaces, the diffusion of metal atoms into the subsurface of oxide has rarely been reported. Moreover, Ar-ion sputtering depth profile experiments demonstrate that there is no Ag which can be detected after the surface Ag particles are removed. Therefore, the diffusion of Ag into the CeO₂(111) subsurface can be ruled out. Desorption of Ag from the CeO₂(111) surface before 800 K is also unlikely because even for a weak Ag-interacted substrate such as Al₂O₃ temperature-programmed desorption (TPD) results demonstrated that Ag desorbs only above 800 K.⁶⁹ Since Ag interacts more strongly with CeO₂ than Al₂O₃, the desorption temperature for Ag on CeO₂(111) must be 800 K or higher. Therefore, desorption temperature for Ag on CeO₂(111) below 800 K is unreasonable. Thus, the decrease in intensity of Ag 3d_{5/2} spectra during annealing before 800 K can be attributed to particle sintering on the surface. Above 800 K, the peak intensity starts to decrease more steeply due to the Ag desorption. By 900 K, all Ag desorbs from the surface, leading to no detectable Ag signal by XPS. The

initial sintering temperature for a low coverage Ag film (0.05 ML) is lower than that for a high coverage film (0.5 ML). This is understandable since the initial particle size is much smaller. Moreover, desorption also completes at lower temperature for a lower coverage. These results are consistent with the fact that small particles desorb more easily than “infinite” particles.⁷⁴

That Ag particles undergo significant sintering on CeO₂(111) before desorption is also confirmed by the observation of the shifts of Ag 3d_{5/2} binding energy as well as by the changes of the full width of half-maximum (fwhm) of the Ag 3d_{5/2} peak. Figure 7(b) displays the binding energy of Ag 3d_{5/2} peaks as a function of annealing temperature for 0.05 and 0.5 ML Ag on CeO₂(111), respectively. As seen, for both Ag coverages, the binding energy of the Ag 3d_{5/2} peak shifts to the lower BE side during annealing. This shift is more apparent for 0.05 ML Ag than for 0.5 ML since the initial particle size is smaller in the former case. In addition, the fwhm (not shown) of the Ag 3d_{5/2} peak decreases during annealing for both coverages. Along with the previous description, the phenomena associated with the changes of BE and fwhm of Ag 3d_{5/2} during annealing are clearly caused by the size effects. Hence, it provides clear evidence for Ag sintering on the CeO₂(111) surface before desorption.

To further prove Ag sintering at elevated temperatures, we performed an experiment of Ag deposition at 500 K. The results show that the increase of Ag signals initially follows the 3D growth mode with a lower number density of particles ($<1 \times 10^{12}$ particles/cm², assuming hemispherical cap growth) than 300 K. This implies that the average particle size at 500 K is larger than at 300 K at a given Ag coverage. Correspondingly, at 500 K a smaller fraction of the substrate area is covered by Ag than at 300 K. However, we cannot rule out the possibility of the lower number of particle density at 500 K caused by a lower sticking probability of Ag on CeO₂(111) as compared to that at 300 K. Similar dependence on the substrate temperature has been observed previously for Cu⁵⁰ and Au^{79–81} grown on TiO₂. Considering the kinetic effects, as the substrate temperature increases, since Ag atoms become more mobile on the surface and some of the kinetic barriers may be surmounted, the Ag particles grow in size by a combination of Ostwald ripening (growth of larger particles at the expense of smaller ones) and coalescence (particles merge together).⁷⁹

4. DISCUSSION

Our results provide clear evidence that the CeO₂(111) surface has been slightly reduced upon Ag deposition. Similar phenomena have also been observed in the growth of Pd, Pt, and Au on ceria.^{24,28,38,42} However, regarding the mechanism of metal-induced reduction of the CeO₂ films, it is still under dispute.^{24,27,42,77,82,83} Summarized from the literature, there are several explanations for metal-induced reduction of CeO₂: (1) charge transfer from the supported metal particles to CeO₂; (2) reverse spillover of lattice oxygen to the surface of the supported metal nanoparticles; (3) metal-catalyzed desorption of surface oxygen atoms; and (4) metal-catalyzed reactions of O atoms from CeO₂ with background CO gas to make CO₂. For the first explanation, for example, Wilson et al.⁷⁷ reported that for Pd/CeO₂ the CeO₂ surface was reduced by electron transfer from the Pd adatoms to the CeO₂ surface. Recently, Škoda et al.⁴² proposed that the formation of a Au–Ce–O gold–ceria interface caused ceria reduction. This finding is consistent with the theoretical study by Shapovalov et al.⁸³ but disagrees with the

experimental results of Baron et al.,²⁶ which strongly suggest that the oxidation state of Au atoms adsorbed on the perfect CeO₂-(111) single-crystal surface is essentially zero. The reduction of ceria caused by the reverse spillover of lattice oxygen to the surface of the supported metal nanoparticles can be found in many literatures.^{18,22,27,38,84–88} For example, Zhdanov and Kasemo⁸⁸ reported that the energy of oxygen atoms on Pt nanoparticles is essentially very close to that in the surface layer of the CeO₂. The activation barrier for reverse spillover from ceria to Pt over the Pt–CeO_x boundary is rather low (10 kcal/mol). Experimental evidence for reverse oxygen spillover on the same system has been reported by Lykhach et al.²⁷ They observed the lattice oxygen migration to the Pt particles while annealing the sample in ultrahigh vacuum (UHV) at temperatures between 400 and 500 K. Other experimental evidence for the oxygen reverse spillover from CeO₂ to supported metal nanoparticles can be found in the case of Rh/CeO₂^{84,85,87} and Pd/CeO₂.⁸² The reduction of CeO₂ caused by metal-catalyzed desorption of surface oxygen atoms was reported by Pfau et al.⁸⁴ for Rh on CeO₂. The reaction of O atoms from CeO₂ with background CO gas to make CO₂, catalyzed by supported metal particles, can also reduce CeO₂, which has been found for Pt on CeO₂.^{28,78}

In the present case of Ag/CeO₂(111), our analysis shows that the final state effects are primarily responsible for the Ag 3d core level binding energy shifts. The small contribution from the initial state effects at very low Ag coverages is attributed to the low average coordination number for Ag atoms of small Ag particles. This means that there is no strong interfacial interaction between Ag and CeO₂(111). When the Ag coverage increases to be higher than 0.5 ML, the contribution from initial state effects to the Ag 3d core level shifts becomes negligible, while the reduction of CeO₂(111) due to Ag adsorption can still be observed when the Ag coverage is above 0.5 ML. This clearly indicates that the reduction of CeO₂(111) does not result from electron transfer from Ag to CeO₂(111). Moreover, Ag has a lower heat of oxide formation and therefore a lower oxygen affinity than cerium;² therefore, it is unreasonable that Ag clusters are oxidized at the Ag/CeO₂ interface. However, it is worth pointing out that our observations do not agree with recent DFT calculations,¹⁸ which indicated that the adsorbed Ag metal atoms becomes oxidized (Ag⁺) by one of the Ce⁴⁺ cations in the underlying oxide.

At room temperature CO does not adsorb on the stoichiometric CeO₂(111) surface, as previously demonstrated by both experimental and theoretical results.^{36,89} We also found that the CeO₂(111) surface is not reduced after leaving the fresh-prepared CeO₂(111) surface in the vacuum chamber for several hours. In other words, the background CO can not be adsorbed on the CeO₂(111) surface at 300 K. A similar experiment was also performed for 0.1 ML Ag covered CeO₂(111). The electronic structure of the surface, e.g., the unoccupied Ce 4f band, shows little change after the sample stays in the vacuum chamber for a long time. This suggests that Ag-catalyzed reaction of O atoms from CeO₂ with background CO to form CO₂, which induces the reduction of CeO₂, does not occur at 300 K.

Having ruled out the possibilities of charge transfer from the supported Ag particles to CeO₂ and Ag-catalyzed reaction of O atoms from CeO₂ with background CO to form CO₂ at 300 K, we attribute the reduction of CeO₂(111) to spillover of lattice oxygen in CeO₂ at the Ag–CeO₂ boundary to the surface of the

supported Ag nanoparticles. This process can happen as long as the CeO₂(111) surface is not completely covered by Ag. This explains well why at higher Ag coverages, before a continuous Ag film is formed, the reduction of CeO₂ can still be observed. One might argue that since the heat of oxide formation of Ag is significantly lower than that of CeO₂, this reverse spillover of oxygen atoms from CeO₂ to Ag nanoparticles less likely occurs. However, Pt has heat of oxide formation similar to Ag,² but as mentioned above, in the nanometer scale the energy of oxygen atoms on Pt nanoparticles does not differ too much from that in the surface layer of the CeO₂; the actual barrier for spillover of O from CeO₂ to Pt is very low.⁸⁸ Therefore, it is reasonable that a similar process might also occur for Ag on CeO₂. These spillovered oxygen atoms on metal nanoparticles might be very reactive, making the Ag/CeO₂ catalysts highly active in the redox reactions. However, we can not rule out the possibility of Ag-catalyzed desorption of surface oxygen atoms from CeO₂ since in our SRPES experiments the intensity of O 1s indeed decreases upon Ag adsorption, although this decrease may be induced only by the damping effects of the Ag adsorbate. It should be mentioned that theoretical calculations might clarify the exact reduction mechanism of CeO₂ upon Ag deposition.

A similar process is also observed when CeO₂ particles are deposited on late transition metals (i.e., so-called inversed model catalysts). There, the CeO₂ is always observed to be slightly reduced by XPS.^{90,91} This effect has also a strong promoting function in CO oxidation on different metal surfaces.

It is interesting that when Ag is deposited onto TiO₂(110) in a way similar to that done here on CeO₂(111) no evidence was seen in the valence band photoemission spectrum for the reduction of the TiO₂ or for Ti³⁺ states (even though Ti³⁺ has a feature similar to the 1.5 eV BE peak seen here for Ce³⁺, when present).⁵⁷ Similarly, no evidence is seen for the reduction of a SnO₂ surface upon Ag deposition.⁹² Thus, the present results show that the CeO₂(111) surface is more easily reduced than both TiO₂ and SnO₂. That it can even be reduced slightly by deposited Ag is somewhat surprising.

5. CONCLUSION

The growth, nucleation, and electronic properties of Ag on the ordered CeO₂(111) thin films grown on Ru(0001) have been systematically studied by SRPES, XPS, and LEED. The results clearly indicate that Ag grows three-dimensionally on the well-ordered CeO₂(111) surface at 300 K. When the CeO₂(111) surface has a high density of defects, Ag populates these defect sites initially, leading to a 2D island growth at low coverages. The binding energy of Ag 3d increases when the Ag particle size decreases, which is mainly due to the final state screening. The interfacial interaction between Ag and CeO₂(111) is weak. Ag particles most likely maintain the metallic state on the CeO₂(111) surface. The slight reduction of the CeO₂(111) surface upon Ag deposition can be ascribed to the reverse spillover of oxygen atoms on CeO₂ at the Ag–CeO₂ boundary to the Ag nanoparticles. Heating the Ag/CeO₂(111) surface leads to the significant sintering of Ag nanoparticles before they completely desorb from the CeO₂(111) surface.

AUTHOR INFORMATION

Corresponding Author

*E-mail: jfzhu@ustc.edu.cn.

ACKNOWLEDGMENT

The authors gratefully acknowledge the financial support from the Natural Science Foundation of China (Grant No. 20873128), the “Hundred Talents Program” of the Chinese Academy of Sciences, the Specialized Research Fund for the Doctoral Program of Higher Education (SRFDP), the Program for New Century Excellent Talents in University (NCET), and National Basic Research Program of China (2010CB923302). CTC acknowledges the US DOE Office of Basic Energy Sciences, Chemical Sciences Division, for partial support of this work.

REFERENCES

- (1) Goodman, D. W. Model catalysts - from extended single-crystals to supported particles. *Surf. Rev. Lett.* **1995**, *2* (1), 9–24.
- (2) Campbell, C. T. Ultrathin metal films and particles on oxide surfaces: Structural, electronic and chemisorptive properties. *Surf. Sci. Rep.* **1997**, *27* (1–3), 1–111.
- (3) Baumer, M.; Freund, H. J. Metal deposits on well-ordered oxide films. *Prog. Surf. Sci.* **1999**, *61* (7–8), 127–198.
- (4) Ernst, K. H.; Ludviksson, A.; Zhang, R.; Yoshihara, J.; Campbell, C. T. Growth-model for metal-films on oxide surfaces - Cu on ZnO-(0001)-O. *Phys. Rev. B* **1993**, *47* (20), 13782–13796.
- (5) Rainer, D. R.; Goodman, D. W. Metal clusters on ultrathin oxide films: model catalysts for surface science studies. *J. Mol. Catal. A: Chem.* **1998**, *131* (1–3), 259–283.
- (6) Lopez, N.; Illas, F.; Pacchioni, G. Adsorption of Cu, Pd, and Cs atoms on regular and defect sites of the SiO₂ surface. *J. Am. Chem. Soc.* **1999**, *121* (4), 813–821.
- (7) Freund, H. J. Model Studies in Heterogeneous Catalysis. *Chem. –Eur. J.* **2010**, *16* (31), 9384–9397.
- (8) Fu, Q.; Wagner, T. Interaction of nanostructured metal overlayers with oxide surfaces. *Surf. Sci. Rep.* **2007**, *62* (11), 431–498.
- (9) Sterrer, M.; Risse, T.; Pozzoni, U. M.; Giordano, L.; Heyde, M.; Rust, H. P.; Pacchioni, G.; Freund, H. J. Control of the charge state of metal atoms on thin MgO films. *Phys. Rev. Lett.* **2007**, *98* (9), 4.
- (10) Haas, G.; Menck, A.; Brune, H.; Barth, J. V.; Venables, J. A.; Kern, K. Nucleation and growth of supported clusters at defect sites: Pd/MgO(001). *Phys. Rev. B* **2000**, *61* (16), 11105–11108.
- (11) Farmer, J. A.; Campbell, C. T. Ceria Maintains Smaller Metal Catalyst Particles by Strong Metal-Support Bonding. *Science* **2010**, *329* (5994), 933–936.
- (12) Boronin, A. I.; Slavinskaya, E. M.; Danilova, I. G.; Gulyaev, R. V.; Amosov, Y. I.; Kumetsov, P. A.; Polukhina, I. A.; Koscheev, S. V.; Zaikovskii, V. I.; Noskov, A. S. Investigation of palladium interaction with cerium oxide and its state in catalysts for low-temperature CO oxidation. *Catal. Today* **2009**, *144* (3–4), 201–211.
- (13) Carrettin, S.; Concepcion, P.; Corma, A.; Nieto, J. M. L.; Puentes, V. F. Nanocrystalline CeO₂ increases the activity of an for CO oxidation by two orders of magnitude. *Angew. Chem., Int. Ed.* **2004**, *43* (19), 2538–2540.
- (14) Trovarelli, A. Catalytic properties of ceria and CeO₂-containing materials. *Catal. Rev.- Sci. Eng.* **1996**, *38* (4), 439–520.
- (15) Park, S. D.; Vohs, J. M.; Gorte, R. J. Direct oxidation of hydrocarbons in a solid-oxide fuel cell. *Nature* **2000**, *404* (6775), 265–267.
- (16) Rodriguez, J. A.; Ma, S.; Liu, P.; Hrbek, J.; Evans, J.; Perez, M. Activity of CeO_x and TiO_x nanoparticles grown on Au(111) in the water-gas shift reaction. *Science* **2007**, *318*, 1757–1760.
- (17) Fu, Q.; Saltsburg, H.; Flytzani-Stephanopoulos, M. Active nonmetallic Au and Pt species on ceria-based water-gas shift catalysts. *Science* **2003**, *301* (5635), 935–938.
- (18) Branda, M. M.; Hernandez, N. C.; Sanz, J. F.; Illas, F. Density Functional Theory Study of the Interaction of Cu, Ag, and Au Atoms with the Regular CeO₂(111) Surface. *J. Phys. Chem. C* **2010**, *114* (4), 1934–1941.
- (19) Zhou, Y. H.; Perket, J. M.; Zhou, J. Growth of Pt Nanoparticles on Reducible CeO₂(111) Thin Films: Effect of Nanostructures and Redox Properties of Ceria. *J. Phys. Chem. C* **2010**, *114* (27), 11853–11860.
- (20) Farmer, J. A.; Baricuatro, J. H.; Campbell, C. T. Ag Adsorption on Reduced CeO₂(111) Thin Films. *J. Phys. Chem. C* **2010**, *114* (40), 17166–17172.
- (21) Lu, J. L.; Gao, H. J.; Shaikhutdinov, S.; Freund, H. J. Gold supported on well-ordered ceria films: nucleation, growth and morphology in CO oxidation reaction. *Catal. Lett.* **2007**, *114* (1–2), 8–16.
- (22) Zhou, J.; Baddorf, A. P.; Mullins, D. R.; Overbury, S. H. Growth and characterization of Rh and Pd nanoparticles on oxidized and reduced CeO_x(111) thin films by scanning tunneling microscopy. *J. Phys. Chem. C* **2008**, *112* (25), 9336–9345.
- (23) Bruix, A.; Neyman, K. M.; Illas, F. Adsorption, Oxidation State, and Diffusion of Pt Atoms on the CeO₂(111) Surface. *J. Phys. Chem. C* **2010**, *114* (33), 14202–14207.
- (24) Wilson, E. L.; Chen, Q.; Brown, W. A.; Thornton, G. CO adsorption on the model catalyst Pd/CeO_{2-x}(111)/Rh(111). *J. Phys. Chem. C* **2007**, *111* (38), 14215–14222.
- (25) Weststrate, C. J.; Westerstrom, R.; Lundgren, E.; Mikkelsen, A.; Andersen, J. N. Influence of Oxygen Vacancies on the Properties of Ceria-Supported Gold. *J. Phys. Chem. C* **2009**, *113* (2), 724–728.
- (26) Baron, M.; Bondarchuk, O.; Stacchiola, D.; Shaikhutdinov, S.; Freund, H. J. Interaction of Gold with Cerium Oxide Supports: CeO₂-(111) Thin Films vs CeO_x Nanoparticles. *J. Phys. Chem. C* **2009**, *113* (15), 6042–6049.
- (27) Lykhach, Y.; Staudt, T.; Lorenz, M. P. A.; Streber, R.; Bayer, A.; Steinruck, H. P.; Libuda, J. Microscopic Insights into Methane Activation and Related Processes on Pt/Ceria Model Catalysts. *ChemPhysChem* **2010**, *11* (7), 1496–1504.
- (28) Mullins, D. R.; Zhang, K. Z. Metal-support interactions between Pt and thin film cerium oxide. *Surf. Sci.* **2002**, *513* (1), 163–173.
- (29) Feng, J.; Chen, J. C.; Xiao, B.; Zhou, X. L.; Yu, J. Electric contact materials of Ag/Y₂O₃ and Ag/CeO₂ synthesized by in situ process. *Rare Met. Mater. Eng.* **2007**, *36* (1), 174–177.
- (30) Wang, J. H.; Liu, M. L.; Lin, M. C. Oxygen reduction reactions in the SOFC cathode of Ag/CeO₂. *Solid State Ionics* **2006**, *177* (9–10), 939–947.
- (31) Bera, P.; Patil, K. C.; Hegde, M. S. NO reduction, CO and hydrocarbon oxidation over combustion synthesized Ag/CeO₂ catalyst. *Phys. Chem. Chem. Phys.* **2000**, *2* (16), 3715–3719.
- (32) Kundakovic, L.; Flytzani-Stephanopoulos, M. Cu- and Ag-modified cerium oxide catalysts for methane oxidation. *J. Catal.* **1998**, *179* (1), 203–221.
- (33) Imamura, S.; Uchihori, D.; Utani, K.; Ito, T. Oxidative Decomposition of Formaldehyde on Silver-Cerium Composite Oxide Catalyst. *Catal. Lett.* **1994**, *24* (3–4), 377–384.
- (34) Aneggi, E.; Llorca, J.; de Leitenburg, C.; Dolcetti, G.; Trovarelli, A. Soot combustion over silver-supported catalysts. *Appl. Catal., B* **2009**, *91* (1–2), 489–498.
- (35) Murrell, L. L.; Carlin, R. T. Silver on ceria: An example of a highly active surface phase oxide carbon oxidation catalyst. *J. Catal.* **1996**, *159* (2), 479–490.
- (36) Aneggi, E.; Llorca, J.; Boaro, M.; Trovarelli, A. Surface-structure sensitivity of CO oxidation over polycrystalline ceria powders. *J. Catal.* **2005**, *234* (1), 88–95.
- (37) Shimizu, K.; Kawachi, H.; Satsuma, A. Study of active sites and mechanism for soot oxidation by silver-loaded ceria catalyst. *Appl. Catal., B* **2010**, *96* (1–2), 169–175.
- (38) Matolin, V.; Johaneck, V.; Skoda, M.; Tsud, N.; Prince, K. C.; Skala, T.; Matolinova, I. Methanol Adsorption and Decomposition on Pt/CeO₂(111)/Cu(111) Thin Film Model Catalyst. *Langmuir* **2010**, *26* (16), 13333–13341.
- (39) Fujimori, A. Mixed-valent ground state of CeO₂. *Phys. Rev. B* **1983**, *28* (4), 2281.

- (40) Mullins, D. R.; Overbury, S. H.; Huntley, D. R. Electron spectroscopy of single crystal and polycrystalline cerium oxide surfaces. *Surf. Sci.* **1998**, *409* (2), 307–319.
- (41) Matsumoto, M.; Soda, K.; Ichikawa, K.; Tanaka, S.; Taguchi, Y.; Jouda, K.; Aita, O.; Tezuka, Y.; Shin, S. Resonant photoemission study of CeO₂. *Phys. Rev. B* **1994**, *50* (16), 11340–11346.
- (42) Skoda, M.; Cabala, M.; Matolinova, I.; Prince, K. C.; Skala, T.; Sutara, F.; Veltruska, K.; Matolin, V. Interaction of Au with CeO₂(111): A photoemission study. *J. Chem. Phys.* **2009**, *130* (3), 7.
- (43) Mullins, D. R.; Radulovic, P. V.; Overbury, S. H. Ordered cerium oxide thin films grown on Ru(0001) and Ni(111). *Surf. Sci.* **1999**, *429* (1–3), 186–198.
- (44) Lu, J. L.; Gao, H. J.; Shaikhutdinov, S.; Freund, H. J. Morphology and defect structure of the CeO₂(111) films grown on Ru(0001) as studied by scanning tunneling microscopy. *Surf. Sci.* **2006**, *600* (22), 5004–5010.
- (45) Weststrate, C. J.; Resta, A.; Westerstrom, R.; Lundgren, E.; Mikkelsen, A.; Andersen, J. N. CO adsorption on a Au/CeO₂(111) model catalyst. *J. Phys. Chem. C* **2008**, *112* (17), 6900–6906.
- (46) Kundakovic, L.; Mullins, D. R.; Overbury, S. H. Adsorption and reaction of H₂O and CO on oxidized and reduced Rh/CeO_x(111) surfaces. *Surf. Sci.* **2000**, *457* (1–2), 51–62.
- (47) Yeh, J. J.; Lindau, I. Atomic subshell photoionization cross sections and asymmetry parameters: 1 ≤ Z <http://www.realliving.com/HER/OH/New-Albany/43054/homes-for-sale/3950-Kitzmilller-Rd-56038375/popup> ≤ 103. *At. Data Nucl. Data Tables* **1985**, *32*, 1–155.
- (48) Seah, M. P.; Dench, W. A. Quantitative Electron Spectroscopy of Surfaces: A Standard Data Base for Electron Inelastic Mean Free Paths in Solids. *Surf. Interface Anal.* **1979**, *1*, 2–11.
- (49) Memeo, R.; Ciccacci, F.; Mariani, C.; Ossicini, S. On the use of the Auger technique for quantitative analysis of overlayers. *Thin Solid Films* **1983**, *109* (2), 159–167.
- (50) Diebold, U.; Pan, J. M.; Madey, T. E. Growth mode of ultrathin copper overlayers on TiO₂(110). *Phys. Rev. B* **1993**, *47* (7), 3868–3876.
- (51) Zhu, J. F.; Farmer, J. A.; Ruzyski, N.; Xu, L.; Campbell, C. T.; Henkelman, G. Calcium adsorption on MgO(100): Energetics, structure, and role of defects. *J. Am. Chem. Soc.* **2008**, *130* (7), 2314–2322.
- (52) Tanuma, S.; Powell, C. J.; Penn, D. R. Calculations of Electron Inelastic Mean Free Paths II. Data for 27 Elements over the 50–2000 eV Range. *Surf. Interface Anal.* **1991**, *17* (13), 911–926.
- (53) Kim, Y. D.; Wei, T.; Wendt, S.; Goodman, D. W. Ag adsorption on various silica thin films. *Langmuir* **2003**, *19* (19), 7929–7932.
- (54) Stracke, P.; Krischok, S.; Kempter, V. Ag-adsorption on MgO: investigations with MIES and UPS. *Surf. Sci.* **2001**, *473* (1–2), 86–96.
- (55) Flank, A. M.; Delaunay, R.; Lagarde, P.; Pompa, M.; Jupille, J. Epitaxial silver layer at the MgO(100) surface. *Phys. Rev. B* **1996**, *53* (4), R1737–R1739.
- (56) Su, C.; Yeh, J. C.; Lin, J. L.; Lin, J. C. The growth of Ag films on a TiO₂(110)-(1 × 1) surface. *Appl. Surf. Sci.* **2001**, *169*, 366–370.
- (57) Luo, K.; St Clair, T. P.; Lai, X.; Goodman, D. W. Silver growth on TiO₂(110)(1 × 1) and (1 × 2). *J. Phys. Chem. B* **2000**, *104* (14), 3050–3057.
- (58) Larsen, J. H.; Ranney, J. T.; Starr, D. E.; Musgrove, J. E.; Campbell, C. T. Adsorption energetics of Ag on MgO(100). *Phys. Rev. B* **2001**, *63*, 19.
- (59) Binns, C. Nanoclusters deposited on surfaces. *Surf. Sci. Rep.* **2001**, *44* (1–2), 1.
- (60) Bagus, P. S.; Brundle, C. R.; Pacchioni, G.; Parmigiani, F. Mechanisms responsible for the shifts of core-level binding energies between surface and bulk atoms of metals. *Surf. Sci. Rep.* **1993**, *19* (3–6), 265–283.
- (61) Mason, M. G. Electronic structure of supported small metal clusters. *Phys. Rev. B (Condens. Matter)* **1983**, *27* (2), 748–762.
- (62) Parmigiana, F.; Kay, E.; Bagus, P. S.; Nelin, C. J. Core binding energies for clusters deposited on different insulating substrates: ESCA spectra and theoretical electronic structure studies. *J. Electron Spectrosc. Relat. Phenom.* **1985**, *36* (3), 257–267.
- (63) Egelhoff, W. F.; Tibbetts, G. G. A photoelectron study of palladium, nickel, and copper clusters on carbon surfaces. *Solid State Commun.* **1979**, *29* (1), 53–57.
- (64) Egelhoff, W. F.; Tibbetts, G. G. Growth of copper, nickel, and palladium films on graphite and amorphous carbon. *Phys. Rev. B* **1979**, *19* (10), S028–S035.
- (65) Lopez-Salido, I.; Lim, D. C.; Dietsche, R.; Bertram, N.; Kim, Y. D. Electronic and geometric properties of Au nanoparticles on highly ordered pyrolytic graphite (HOPG) studied using X-ray Photoelectron Spectroscopy (XPS) and Scanning Tunneling Microscopy (STM). *J. Phys. Chem. B* **2006**, *110* (3), 1128–1136.
- (66) Wagner, C. D. Auger lines in X-ray photoelectron spectroscopy. *Anal. Chem.* **1972**, *44* (6), 967–973.
- (67) Wagner, C. D. Auger parameter in electron spectroscopy for the identification of chemical species. *Anal. Chem.* **1975**, *47* (7), 1201–1203.
- (68) Wagner, C. D.; Gale, L. H.; Raymond, R. H. Two-dimensional chemical state plots: a standardized data set for use in identifying chemical states by X-ray photoelectron spectroscopy. *Anal. Chem.* **1979**, *51* (4), 466–482.
- (69) Luo, K.; Lai, X.; Yi, C. W.; Davis, K. A.; Gath, K. K.; Goodman, D. W. The growth of silver on an ordered alumina surface. *J. Phys. Chem. B* **2005**, *109* (9), 4064–4068.
- (70) Andersen, J. N.; Hennig, D.; Lundgren, E.; Methfessel, M.; Nyholm, R.; Scheffler, M. Surface core-level shifts of some 4d-metal single-crystal surfaces: Experiments and ab initio calculations. *Phys. Rev. B* **1994**, *50* (25), 17525.
- (71) Kim, H. Corrosion process of silver in environments containing 0.1 ppm H₂S and 1.2 ppm NO₂. *Mater. Corros.* **2003**, *54*, 243–250.
- (72) Guo, D. H.; Guo, Q. L.; Zheng, K. F.; Wang, E. G.; Bao, X. H. Initial growth and oxygen adsorption of silver on Al₂O₃ film. *J. Phys. Chem. C* **2007**, *111* (10), 3981–3985.
- (73) Sarode, P. R.; Priolkar, K. R.; Bera, P.; Hegde, M. S.; Emura, S.; Kumashiro, R. Study of local environment of Ag in Ag/CeO₂ catalyst by EXAFS. *Mater. Res. Bull.* **2002**, *37* (9), 1679–1690.
- (74) Rodriguez, J. A.; Kuhn, M.; Hrbek, J. Interaction of silver, cesium, and zinc with alumina surfaces: Thermal desorption and photoemission studies. *J. Phys. Chem.* **1996**, *100* (46), 18240–18248.
- (75) Hüfner, S.; Wertheim, G. K.; Wernick, J. H. X-Ray Photoelectron Spectra of the Valence Bands of Some Transition Metals and Alloys. *Phys. Rev. B* **1973**, *8* (10), 4511.
- (76) Vijayakrishnan, V.; Chainani, A.; Sarma, D. D.; Rao, C. N. R. Metal-insulator transitions in metal clusters: a high-energy spectroscopy study of palladium and silver clusters. *J. Phys. Chem.* **1992**, *96* (22), 8679–8682.
- (77) Wilson, E. L.; Grau-Crespo, R.; Pang, C. L.; Cabailh, G.; Chen, Q.; Purton, J. A.; Catlow, C. R. A.; Brown, W. A.; de Leeuw, N. H.; Thornton, G. Redox behavior of the model catalyst Pd/CeO_{2-x}/Pt(111). *J. Phys. Chem. C* **2008**, *112* (29), 10918–10922.
- (78) Zarraga-Colina, J.; Nix, R. M. Fabrication of model Pt-ceria catalysts and an analysis of their performance for CO oxidation. *Surf. Sci.* **2006**, *600* (15), 3058–3071.
- (79) Zhang, L.; Persaud, R.; Madey, T. E. Ultrathin metal films on a metal oxide surface: Growth of Au on TiO₂ (110). *Phys. Rev. B* **1997**, *56* (16), 10549–10557.
- (80) Zhang, L.; Cosandey, F.; Persaud, R.; Madey, T. E. Initial growth and morphology of thin Au films on TiO₂(110). *Surf. Sci.* **1999**, *439* (1–3), 73–85.
- (81) Marques, H. P.; Canario, A. R.; Moutinho, A. M. C.; Teodoro, O. M. N. D. Shaping Ag clusters on titania. *J. Phys.: Conf. Ser.* **2007**, *775*–9.
- (82) Smirnov, M. Y.; Graham, G. W. Pd oxidation under UHV in a model Pd/ceria-zirconia catalyst. *Catal. Lett.* **2001**, *72* (1–2), 39–44.
- (83) Shapovalov, V.; Metiu, H. Catalysis by doped oxides: CO oxidation by Au_xCe_{1-x}O₂. *J. Catal.* **2007**, *245* (1), 205–214.
- (84) Pfau, A.; Schierbaum, K. D.; Gopel, W. The electronic structure of CeO₂ thin films: the influence of Rh surface dopants. *Surf. Sci.* **1995**, *331*, 1479–1485.

(85) Galdikas, A.; Descorme, C.; Duprez, D. Surface diffusion upon oxygen isotopic exchange on oxide-supported metal nanoclusters. *Solid State Ionics* **2004**, *166* (1–2), 147–155.

(86) Christou, S. Y.; Efstathiou, A. M. Effects of Pd particle size on the rates of oxygen back-spillover and CO oxidation under dynamic oxygen storage and release measurements over Pd/CeO₂ catalysts. *Top. Catal.* **2007**, *42–43* (1–4), 351–355.

(87) Descorme, C.; Duprez, D. Oxygen surface mobility and isotopic exchange on oxides: role of the nature and the structure of metal particles. *Appl. Catal., A* **2000**, *202* (2), 231–241.

(88) Zhdanov, V. P.; Kasemo, B. Kinetic models of oxygen supply from CeO_x to active nanometer particles of three-way catalysts. *Appl. Surf. Sci.* **1998**, *135* (1–4), 297–306.

(89) Nolan, M.; Watson, G. W. The surface dependence of CO adsorption on ceria. *J. Phys. Chem. B* **2006**, *110* (33), 16600–16606.

(90) Suchorski, Y.; Wrobel, R.; Becker, S.; Weiss, H. CO Oxidation on a CeO_x/Pt(111) Inverse Model Catalyst Surface: Catalytic Promotion and Tuning of Kinetic Phase Diagrams. *J. Phys. Chem. C* **2008**, *112*, 20012–20017.

(91) Wrobel, R.; Suchorski, Y.; Becker, S.; Weiss, H. Cerium oxide layers on the Cu(111) surface: Substrate-mediated redox properties. *Surf. Sci.* **2008**, *602* (2), 436–442.

(92) DePadova, P.; Larciprete, R.; Mangiantini, M.; Fanfoni, M. Cr, Sn and Ag/SnO₂ interface formation studied by synchrotron radiation induced UPS. *J. Electron Spectrosc. Relat. Phenom.* **1995**, *76*, 499–504.